AIP | Review of Scientific Instruments

High sensitivity magnetic imaging using an array of spins in diamond

S. Steinert, F. Dolde, P. Neumann, A. Aird, B. Naydenov, G. Balasubramanian, F. Jelezko, and J. Wrachtrup

Citation: Review of Scientific Instruments **81**, 043705 (2010); doi: 10.1063/1.3385689
View online: http://dx.doi.org/10.1063/1.3385689
View Table of Contents: http://scitation.aip.org/content/aip/journal/rsi/81/4?ver=pdfcov
Published by the AIP Publishing

High sensitivity magnetic imaging using an array of spins in diamond

S. Steinert,[a] F. Dolde, P. Neumann, A. Aird, B. Naydenov, G. Balasubramanian, F. Jelezko, and J. Wrachtrup
3. Physikalisches Institut, Universität Stuttgart, Pfaffenwaldring 57, 70550 Stuttgart, Germany

(Received 2 February 2010; accepted 17 March 2010; published online 23 April 2010)

We present a solid state magnetic field imaging technique using a two-dimensional array of spins in diamond. The magnetic sensing spin array is made of nitrogen vacancy (NV) centers created at shallow depths. Their optical response is used for measuring external magnetic fields in close proximity. Optically detected magnetic resonance is read out from a 60×60 μm^2 field of view in a multiplexed manner using a charge coupled device camera. We experimentally demonstrate full two-dimensional vector imaging of the magnetic field produced by a pair of current carrying microwires. The presented wide-field NV magnetometer offers, in addition to its high magnetic sensitivity and vector reconstruction, an unprecedented spatiotemporal resolution and functionality at room temperature. © *2010 American Institute of Physics.* [doi:10.1063/1.3385689]

I. INTRODUCTION

Sensing and imaging magnetic fields has been developed extensively during the past few decades, propelled by applications ranging from medical to materials science. A wealth of methods has been developed to sense and image magnetic fields with high resolution and sensitivity. Magnetic resonance imaging (MRI), an indispensable tool in clinical diagnostics, would have revolutionary impact if the sensitivity could be improved to image live cells with subcellular resolutions. The inherent limitation arises from the conventional inductive detection that results in a poor signal to noise ratio.

Alternative detection techniques using superconducting quantum interference devices,[1] magnetic resonance force microscopy,[2,3] and alkali vapor atomic magnetometers[4,5] have been explored. Though these methods offer high sensitivity, they require cryogenic cooling, vacuum conditions, or prolonged data acquisition, and are therefore limited to special applications.

Alternatively, a proximal single nitrogen vacancy (NV) center in diamond as magnetic sensing probe showed promising results.[6–10] The NV defect center has several outstanding advantages for this application. Optical polarization and spin state readout facilitates convenient and noninvasive far field detection.[11] Furthermore, the atomic NV sensor permits the minimization of the sample-sensor distance, while the long spin coherence in the nearly spin-free diamond lattice provides ultrasensitive magnetic field detection.[7] The disadvantages of using a single NV for magnetic imaging are limited magnetic sensitivity, restricted vector reconstruction, and the inherently slow point-scanning data acquisition. Here, we demonstrate an enhanced magnetic imaging technique with an ensemble of NV centers acting as magnetic field sensors combined with rapid charge coupled device (CCD) camera-based image detection of a large field of view. The technique offers full reconstruction of the magnetic field vector, improved temporal resolution, and enhanced field sensitivity under ambient conditions.

II. PRINCIPLE AND SETUP

The NV center in diamond consists of a substitutional nitrogen atom adjacent to a carbon vacancy [Fig. 1(a)]. Its two unpaired electrons form a spin triplet in the electronic ground state (^3A), while the degenerated $m_s=\pm1$ sublevels are separated from $m_s=0$ by 2.87 GHz [Fig. 1(b)]. The $m_s=0$ sublevel exhibits a high fluorescence rate when optically pumped. In contrast, when the center is excited in the $m_s=\pm1$ levels, the NV exhibits a higher probability to cross over to the nonradiative singlet state (^1A) followed by a subsequent relaxation into $m_s=0$. As a result, the spin state can be optically read out with a fluorescent contrast of ~30% ($m_s=0$ "bright," $m_s=\pm1$ "dark").[11] When an external magnetic field is applied, the degeneracy of the spin sublevels $m_s=\pm1$ is lifted via Zeeman splitting. This causes the resonance lines to split depending on the applied magnetic field magnitude and its direction. This dependency is used in the present work for vector magnetometry as the resonant spin transitions can be probed by sweeping the microwave (MW) frequency resulting in characteristic dips in the optically detected magnetic resonance (ODMR) spectrum [Fig. 2(a)].

Instead of using a single NV center as field sensor, we employed ion implantation to create a homogenous layer of negatively charged NV centers into an ultrapure [100] type IIa diamond (Element Six). The ensemble NV sensor offers a higher magnetic sensitivity which scales with $\sqrt{N}$ due to the amplified fluorescence signal from N sensing spins. Another advantage is the improved vector reconstruction since the diamond lattice imposes four distinct tetrahedral NV orientations [Fig. 2(b)]. The magnetic field projections along each of these axes are measured as a single composite spectrum and a numerical algorithm developed in this study is used to reconstruct the full magnetic field vector. The magnitude B and orientation (θ_B, φ_B) of the external magnetic field was

[a]Author to whom correspondence should be addressed. Electronic mail: s.steinert@physik.uni-stuttgart.de.

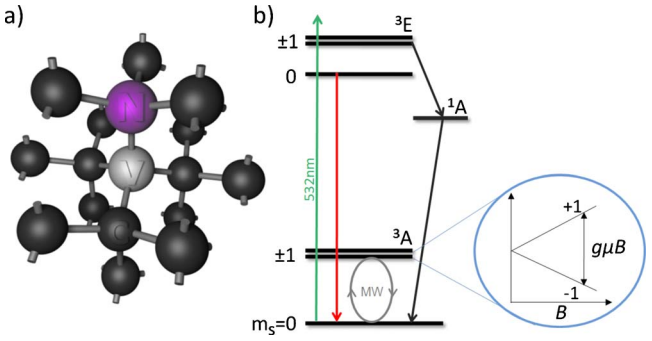

FIG. 1. (Color online) (a) The NV center in diamond consists of a substitutional nitrogen atom (N) associated with a vacancy (V). (b) Energy level scheme of the NV. The electron spin resonance transition between $m_s=0$ and $m_s=\pm 1$ is changed via Zeeman splitting by an external magnetic field B which lifts the degeneracy of $m_s=\pm 1$ (circled inset). Probing the resonant spin transitions is achieved via application of MW fields enabling the detection of the external magnetic field.

calculated by analyzing the ODMR spectra of each pixel individually based on an unconstrained least-square algorithm using custom written MATLAB codes (Mathworks). First, we precisely determined the center frequencies of the experimental resonance transitions in the ODMR spectra ($\upsilon_{\text{ODMR-Fit}}$). Second, we solved the eigenvalues of the diagonalized Hamiltonian H_i for each NV axis using random initial input parameters $(B_0, \theta_{B,0}, \varphi_{B,0})$, which allows the calculation of all resonant transitions for a given external field[12]

$$H_i = D \cdot \hat{d}_i + g_e \mu_B B(\sin\,\theta_B \cdot \cos\,\varphi_B \cdot \hat{S}_x + \sin\,\theta_B \cdot \sin\,\varphi_B \cdot \hat{S}_y + \cos\,\varphi_B \cdot \hat{S}_z), \quad (1)$$

where $\hat{d}_i$ is the fine structure tensor for each of the four NV orientations, $\hat{S}_x, \hat{S}_y, \hat{S}_z$ are the electron spin matrices, D is the zero field splitting between the spin sublevels, g_e the electron g-factor, and μ_B is the Bohr magneton. These calculated resonance transition ($\upsilon_{\text{Iteration}}$) were used to compute an error criterion χ according to

$$\chi = \sum (\nu_{\text{ODMR-Fit}} - \nu_{\text{Iteration}})^2. \quad (2)$$

Then, we iteratively changed the field parameters (B, θ_B, φ_B) until the error χ converged to a minimum. This procedure was repeated ten times with random initial input parameters. The final solution for the magnetic field vector of each pixel was determined by the solution with the minimal square error of all ten iterations. However, C_{3v} symmetry of the NV center imposes a set of four possible indistinguishable vectors if the field is aligned to one NV axis while maximal 24 possible vector orientations exist if the field is not aligned to any NV axis.[12] From this set, the correct orientation can be recovered by applying a tiny bias field along one preferred axis and monitoring corresponding perturbation on the others. Alternatively, having an *a priori* knowledge of the magnetic field direction, the NV sensor can be placed in such a manner that the vector outcome would be distinct.

In order to demonstrate full vector reconstruction of our wide-field magnetometer, we fabricated gold microwires on

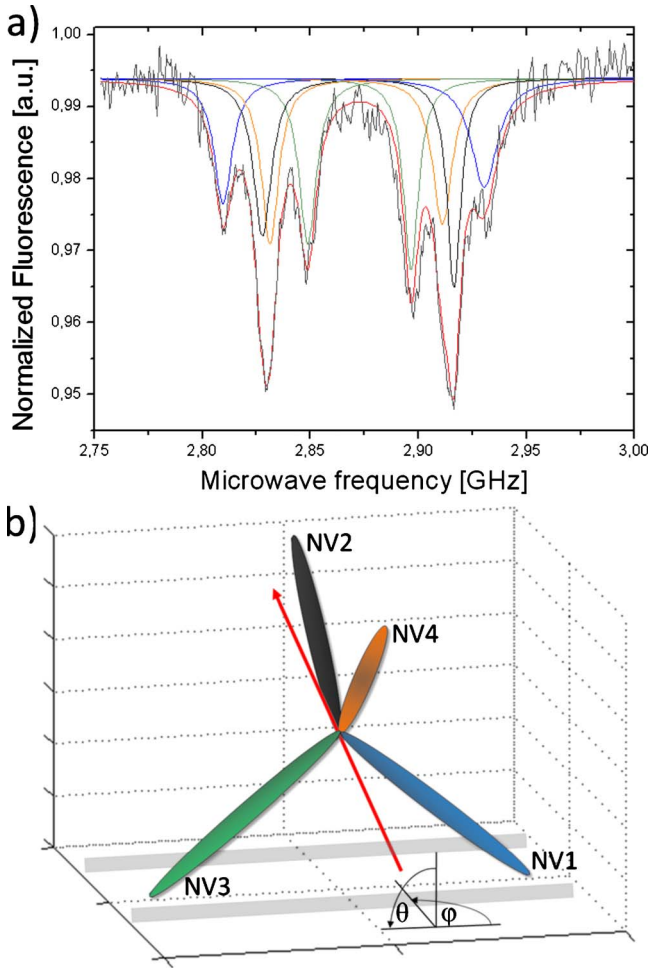

FIG. 2. (Color online) (a) Characteristic ensemble ODMR spectrum from a single pixel. The fitted ODMR spectrum reveals the precise position of the four individual pairs of resonant transitions of each NV axis [see corresponding NV 1–4 in (b)]. For this ODMR spectrum, the external magnetic field can be estimated to be B=2.7 mT, θ_B=17.7°, and φ_B=6.8° [arrow in (b)]. (b) Orientation of the four crystallographic NV axes in a [100] diamond crystal. The orientation of the two microwires (gray stripes) is aligned along the NV1-NV3 axis.

top of the diamond and imaged the magnetic field distribution created by 75 mA dc currents through the wires (see Fig. 3). Optical excitation is achieved using a 532 nm laser (Verdi, Coherent) set to wide-field illumination by focusing the laser onto the back-focal plane of the objective (60×, 1.49 NA, Olympus). The two-dimensional fluorescence is projected onto a 512×512 pixel CCD camera (Cascade 512B, Roper Scientific) detecting the entire image at once with an integration time of only 100 ms. Our optics yield an effective pixel size of ~100 nm with a field of view of ~60×60 μm^2. The camera is synchronized to the MW source (SMIQ 03B, Rohde & Schwarz) which is swept from 2.7 to 3 GHz in steps of 500. Thus, we acquire an image stack within 75 s where each image represents the response of the NV sensor at a given MW frequency kHz. This multiplexed data acquisition of a large field of view is a substantial improvement compared to slow point-scanning methods since each pixel contains the spatial information about the external magnetic field.

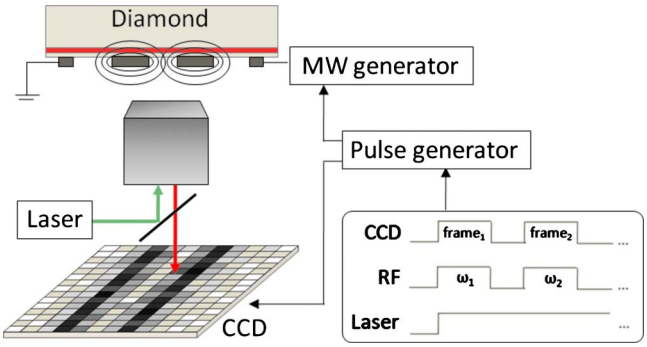

FIG. 3. (Color online) Wide-field magnetic imaging setup. The shallow implanted NV centers (rectangular layer) in diamond sense the magnetic field created by dc currents passing through the two inner wires with the same polarity (gray rectangles with black ellipses representing the magnetic field lines). Optical readout is achieved by continuously exciting the NV sensor with green laser light set to wide-field illumination, sweeping the MW and simultaneously detecting the entire field of view using a CCD camera.

III. RESULTS

In a first step, we created the NV sensor by homogenously implanting $^{15}N^+$ ions with 4 keV per atom into the diamond. The implanted nitrogen atoms have a mean depth of 6.7 ± 2.8 nm [Fig. 4(a)] and are subsequently converted to NV centers by annealing the sample at 800 °C under high vacuum. This thin layer of magnetic sensing NVs permits precise detection of magnetic fields located in very close proximity to the actual NV sensor. Higher NV densities have several advantages: Shorter integration times due to higher signal-to-noise ratio and enhanced sensitivity to magnetic fields. However, the nitrogen content in diamond increases with the implantation dosage due to the imperfect conversion efficiency from implanted nitrogen to NV. Since nitrogen is a paramagnetic impurity capable of dipolar coupling to the NV, elevated nitrogen content leads to dephasing and ultimately to reduced sensitivity. In order to assess the effect of higher implantation dosages on the magnetometer's performance, we varied the implantation density and analyzed the line width and signal of the ODMR spectra in zero-field. As shown in Fig. 4(b), a nitrogen induced broadening of the line width was observed for higher implantation dosages. On the other hand, assuming that the magnetometer achieved the desired sensitivity, higher NV densities facilitate substantially faster ODMR readout due to the elevated fluorescence signal. Therefore, depending on the experimental requirements, a compromise is required between sensitivity and acquisition speed.

For the following experiments, we used an intermediate nitrogen implantation dosage with ~1000 NV centers per μm^2. This ensemble density facilitates a sensitive detection with an integration time per 512×512 pixel frame of only 100 ms.

In order to show that this homogenously implanted NV sensor can be used as an efficient vector magnetometer, we optically detected the resonance transitions of the NV array sensing the magnetic field created by dc current carrying microwires. Subsequently, each pixel was subjected to an iterative reconstruction of the magnetic field. The experimentally extracted magnetic field amplitude agrees well with the numerical simulation [Fig. 5(a)]. In the middle section, the fields of each wire are in opposite direction and counteract each other. The reason that both fields do not cancel out completely is due to the fact that the actual NV sensors are about 2 μm below the center of the microwires. Thus, the B_x components perpendicular to the wire are additive. The iterative algorithm also reconstructs the orientation of the external magnetic field. For demonstration purposes, we deliberately placed the microwires along two NV projections, hence NV1 and NV3 are parallel to the magnetic field as illustrated in Fig. 2(b). In principle, it is not possible to distinguish the directionality of the magnetic field without applying a second known bias field. However, in our experimental setup, the field is aligned along NV1 corresponding to $\varphi_B = 0°$ for all pixels as the polarity of the current is the same for both wires. The unconstrained iterative algorithm detects the expected Gaussian distribution along this NV axis for all pixels

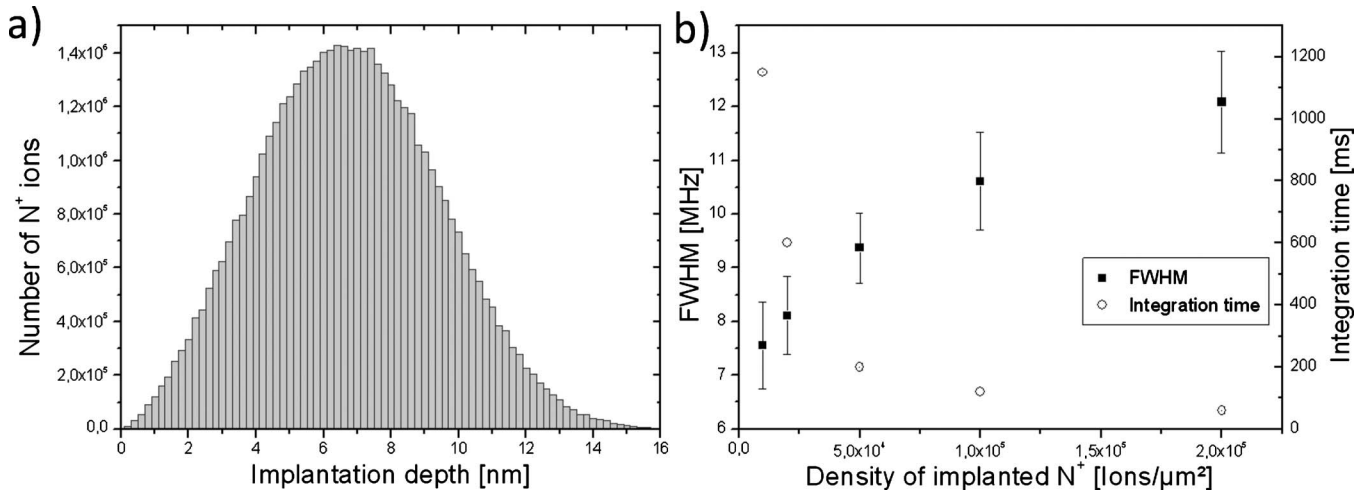

FIG. 4. (a) Implantation depth profile of the implanted nitrogen ions. The data are based on a Monte Carlo simulation using the SRIM package. (b) Fitted line width of the resonance peak without an external magnetic field (black rectangles; error bar represents standard deviation). Though the FWHM increased with higher NV density, significantly shorter exposure times are possible for CCD integration (dotted circles). Exposure times were set to match the same total photon counts as the highest implantation dosage.

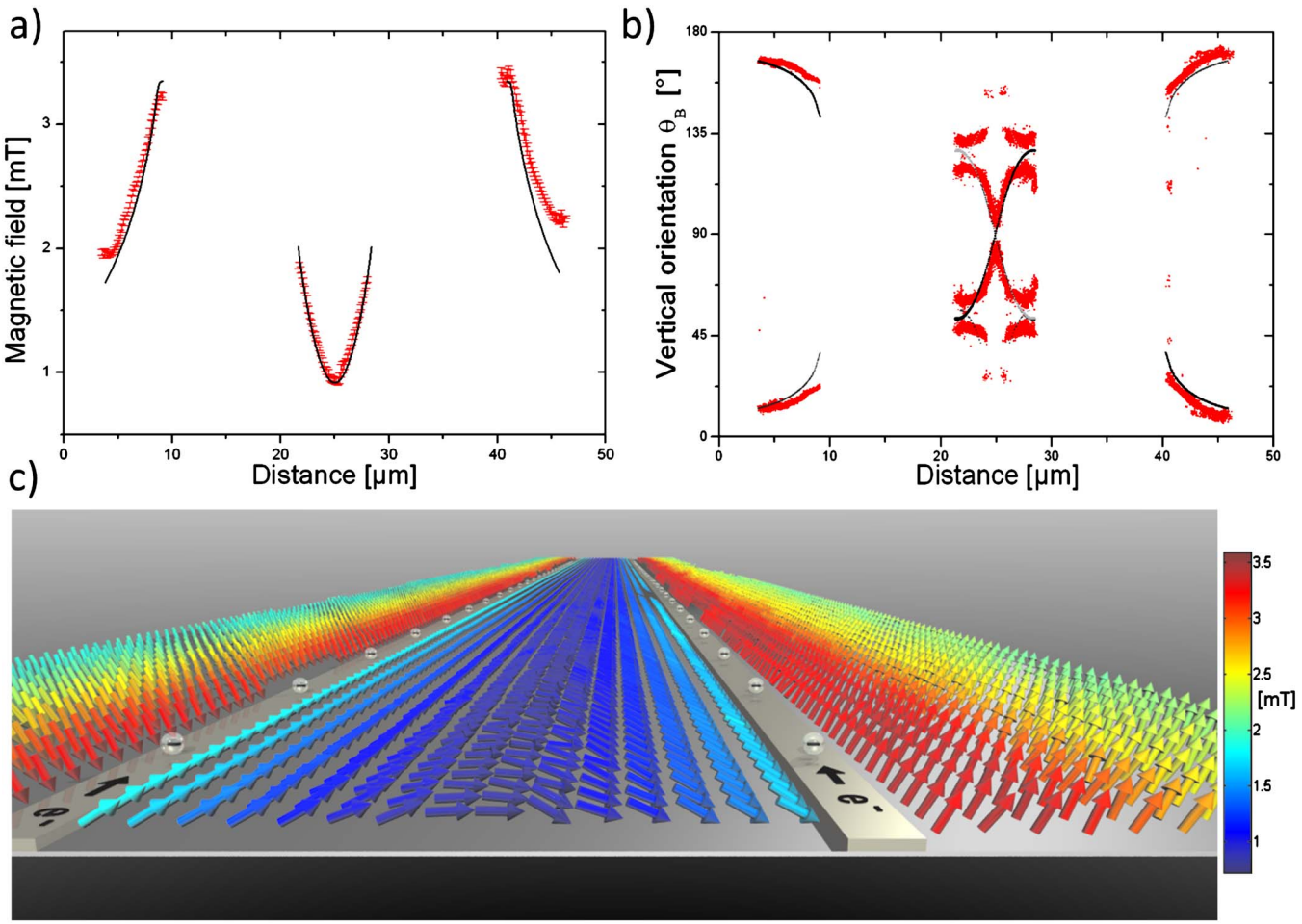

FIG. 5. (Color online) (a) Cross-section of the measured magnetic field averaged along the entire wire length. The magnetic field was numerically simulated (black lines) and iteratively calculated (error bars representing standard deviation). The two wires are located at 10–20 and 30–40 μm, respectively. (b) Cross-section of the simulated (black curve) and experimental evolution of θ_B (circles). The exact solution is superimposed by a second set of possible outcomes (gray line) due to the second NV projection which is also horizontally aligned to the magnetic field. For the simulation, we assumed φ to be aligned to the NV projection ($\varphi_B=0° \pm 10°$) and analogously plotted the corresponding measured θ_B solutions. (c) Pixelwise measured magnetic field (B, θ_B, φ_B) produced by two current carrying wires. Data points perpendicular to the wires were binned by a factor of 3 and wire dimensions were downsized for representational purposes only. The plotted data were extracted from results previously shown, but θ_B angles were projected according to the right-hand rule for both wires [see black line in (b)].

with an initial guess $\varphi_{\text{init}}=0°$. The circular orientation of the magnetic field around each wire leads to a distance dependent θ_B. The exact and numerically calculated course of θ_B is illustrated by the black curve in Fig. 5(b). The superposition with the blue curve is due to the crystal symmetry of the two horizontally aligned NV projections NV1 and NV3 with a vertical symmetry along $\theta_B=90°$. Apart from slight deviations, it is evident that the experimentally obtained vertical angles follow the predicted values. Thus, it is possible to regain the correct magnitude as well as the orientation of the external magnetic field. Though this iterative process is limited in terms of full vector reconstruction due to symmetry effects in diamond, it is possible to recover the true magnetic field vector. For our experimental setup, all θ angles can be projected to the correct NV axis according to the right-hand rule [see black line in Fig. 5(b)]. The resulting pixelwise calculated magnetic vector field is illustrated in Fig. 5(c).

IV. SUMMARY AND OUTLOOK

To summarize, we implemented the first imaging vector magnetometer using an array of NV spins combined with a fast camera readout. The minimum detectable field scales with $\sigma/\sqrt{\text{N}}$, where σ is the accuracy of fitting the resonant transitions in the ODMR spectrum and N is the number of photons contributing to the informative ODMR contrast. With typical values of $\sigma=420$ kHz and $\text{N}=91\,000$ s^{-1}, our ensemble magnetometer achieves an experimental magnetic sensitivity of 20 $\text{nT}/\sqrt{\text{Hz}}$. This high magnetic sensitivity together with a spatial resolution of 250 nm and functionality under ambient conditions renders our wide-field NV magnetometer a prime candidate for a variety of applications in science and technology. Imaging magnetic signatures of nanoscopic objects in a snapshot type imaging offers the possibility to study the dynamics with high temporal resolution. One practical application for such sensitive magnetic field detection is to perform MRI at the microscopic scale or to

probe ionic fluctuations across single membrane channels.[13] Multiplexed magnetic imaging of ion flows enables a label-free approach in imaging cellular activity with optical resolution. Considerable potential for further sensitivity enhancements resides in coherent spin manipulation techniques exploiting the longer phase memory times and enhanced readout fidelities.[7,14–16]

ACKNOWLEDGMENTS

This work was supported by the EU (DINAMO 245122), DFG (Spin microscope WR28/16-2), and the Landesstiftung BW (Internationale Spitzenforschung P-LSSPII/11). Financial support by the Max-Planck-Gesellschaft is acknowledged.

[1] R. McDermott, S. K. Lee, B. ten Haken, A. H. Trabesinger, A. Pines, and J. Clarke, Proc. Natl. Acad. Sci. U.S.A. **101**, 7857 (2004).
[2] D. Rugar, R. Budakian, H. J. Mamin, and B. W. Chui, Nature (London) **430**, 329 (2004).
[3] C. L. Degen, M. Poggio, H. J. Mamin, C. T. Rettner, and D. Rugar, Proc. Natl. Acad. Sci. U.S.A. **106**, 1313 (2009).
[4] M. P. Ledbetter, I. M. Savukov, D. Budker, V. Shah, S. Knappe, J. Kitching, D. J. Michalak, S. Xu, and A. Pines, Proc. Natl. Acad. Sci. U.S.A. **105**, 2286 (2008).
[5] S. Xu, V. V. Yashchuk, M. H. Donaldson, S. M. Rochester, D. Budker, and A. Pines, Proc. Natl. Acad. Sci. U.S.A. **103**, 12668 (2006).
[6] G. Balasubramanian, I. Y. Chan, R. Kolesov, M. Al-Hmoud, J. Tisler, C. Shin, C. Kim, A. Wojcik, P. R. Hemmer, A. Krueger, T. Hanke, A. Leitenstorfer, R. Bratschitsch, F. Jelezko, and J. Wrachtrup, Nature (London) **455**, 648 (2008).
[7] G. Balasubramanian, P. Neumann, D. Twitchen, M. Markham, R. Kolesov, N. Mizuochi, J. Isoya, J. Achard, J. Beck, J. Tissler, V. Jacques, P. R. Hemmer, F. Jelezko, and J. Wrachtrup, Nature Mater. **8**, 383 (2009).
[8] C. L. Degen, Appl. Phys. Lett. **92**, 243111 (2008).
[9] J. R. Maze, P. L. Stanwix, J. S. Hodges, S. Hong, J. M. Taylor, P. Cappellaro, L. Jiang, M. V. G. Dutt, E. Togan, A. S. Zibrov, A. Yacoby, R. L. Walsworth, and M. D. Lukin, Nature (London) **455**, 644 (2008).
[10] J. M. Taylor, P. Cappellaro, L. Childress, L. Jiang, D. Budker, P. R. Hemmer, A. Yacoby, R. Walsworth, and M. D. Lukin, Nat. Phys. **4**, 810 (2008).
[11] A. Gruber, A. Drabenstedt, C. Tietz, L. Fleury, J. Wrachtrup, and C. v. Borczyskowski, Science **276**, 2012 (1997).
[12] See supplementary material at http://dx.doi.org/10.1063/1.3385689 for detailed explanation of Hamiltonian matrices and ambiguity of vector reconstruction.
[13] L. T. Hall, J. H. Cole, C. D. Hill, and L. C. L. Hollenberg, Phys. Rev. Lett. **103**, 220802 (2009).
[14] V. M. Acosta, E. Bauch, M. P. Ledbetter, C. Santori, K. M. C. Fu, P. E. Barclay, R. G. Beausoleil, H. Linget, J. F. Roch, F. Treussart, S. Chemerisov, W. Gawlik, and D. Budker, Phys. Rev. B **80**, 115202 (2009).
[15] M. Steiner, J. Beck, P. Neumann, F. Jelezko, and J. Wrachtrup, Phys. Rev. B **81**, 035205 (2010).
[16] M. Mehring and V. Weberrub, *Object-Oriented Magnetic Resonance: Classes and Objects, Calculations and Computations* (Academic, New York, 2006).